AIAA JOURNAL
Vol. 36, No. 6, June 1998

Numerical Study of Scram Accelerator Starting Characteristics

Jeong-Yeol Choi,* In-Seuck Jeung,† and Youngbin Yoon‡
Seoul National University, Seoul 151-742, Republic of Korea

A numerical study is carried out to investigate the ignition and the detonation initiation process in a scram accelerator operating at a superdetonative mode. To simulate the scram accelerator launching process, a conical projectile is considered, injected with an initial velocity of 2500 m/s from the 1 atm air into a 25 atm $2H_2 + O_2 + mN_2$ mixture. As a dilution gas, nitrogen is selected and assumed to be inert. The time accurate solutions of Reynolds averaged Navier–Stokes equations for chemically reacting flows are obtained by using a point-implicit method and an upwind-biased third-order scheme with a steady-state solution for airflow as an initial condition. To examine combustion characteristics and ram-accelerator operation limits, mixture compositions are varied from $2H_2 + O_2 + 3.76N_2$ to $2H_2 + O_2 + 9N_2$ by changing the amount of N_2. The flowfield results show the detailed ignition mechanism, the initiation process of the oblique detonation, and the starting characteristics of the scram accelerator. The results also identify clearly the combustion characteristics of the operational failures at lower and upper dilution limits that have been observed in experiments. The visualized flow results of the present simulation provide a better understanding of the supersonic reacting flow in a scram accelerator.

Introduction

A RAM accelerator is a concept using the principle of ramjet propulsion as a propelling mechanism of a projectile in a barrel[1,2]; a combustible mixture gas is compressed by a series of shocks and then generates thrust force by a high-speed combustion mechanism such as an oblique detonation. Even though there are several modes of ram accelerator operation, typical ones are the thermally choked mode and the superdetonative mode. In the thermally choked mode, which is adequate for subdetonative operation, much experimental research, as well as theoretical and numerical research has been done and a number of technical advances have been achieved in many research facilities.[3–9] In the superdetonative mode ram accelerator, which is called the supersonic combustion ram (scram) accelerator, supersonic combustion is accomplished by an oblique detonation around the midsection of the projectile and thrust is obtained by the expansion of the burned gas along the tail shaped as a conical nozzle. As the velocity of a ram-projectile is enormously high, the internal flow in the scram accelerator has a very high Mach number and Reynolds number with very fast but finite rate chemical reactions. In addition, the supersonic reacting flow may show transient features during the starting process as ignition occurs and the detonation wave propagates. However, only a few experimental studies have been done in this mode,[10] and the combustion mechanism of the scram accelerator remains to be confirmed despite much research on the related shock-induced combustion phenomena and the stability of the oblique detonation.[11–20]

Especially, there has not been an intensive study on the ignition process and the resulting unstart phenomena during the injection process from the launcher to the accelerator barrel,[10] which might be important in determining the operational limit of the scram accelerator. Therefore, the direct initiation of the superdetonative mode operation and its combustion process were analyzed in this study by carrying out unsteady Navier–Stokes numerical simulations. For the simulation of the scram accelerator launching process, a conical projectile is considered to be injected with an initial velocity of 2500 m/s from 1 atm air into pressurized $2H_2 + O_2 + mN_2$ mixtures. A computational domain is attached to the projectile and is assumed to move with the velocity variation that is calculated from the external thrust force evaluated by integrating the axial component of the pressure and shear stress over the projectile surface.

Governing Equations

Navier–Stokes Equations for Supersonic Reacting Flow

To analyze the chemically reacting supersonic viscous flow in a ram accelerator, the fully coupled form of species conservation equations and Reynolds averaged Navier–Stokes equations is considered over the axisymmetric geometry. The governing equations for a number of N species are summarized in a conservative vector form in general curvilinear (ξ, η) coordinates:

$$\frac{1}{J}\frac{\partial \boldsymbol{Q}}{\partial t} + \frac{\partial \boldsymbol{F}}{\partial \xi} + \frac{\partial \boldsymbol{G}}{\partial \eta} + \frac{1}{J}\boldsymbol{H} = \frac{1}{J}\boldsymbol{W} + \frac{\partial \boldsymbol{F}_v}{\partial \xi} + \frac{\partial \boldsymbol{G}_v}{\partial \eta} + \frac{1}{J}\boldsymbol{H}_v \tag{1}$$

where

$$\boldsymbol{Q} = \begin{bmatrix} \rho_1 \\ \rho_2 \\ \vdots \\ \rho_N \\ \rho u \\ \rho v \\ e \end{bmatrix}, \quad \boldsymbol{F} = \frac{1}{J}\begin{bmatrix} \rho_1 U \\ \rho_2 U \\ \vdots \\ \rho_N U \\ \rho u U + \xi_x p \\ \rho v U + \xi_y p \\ U(e+p) \end{bmatrix}, \quad \boldsymbol{G} = \frac{1}{J}\begin{bmatrix} \rho_1 V \\ \rho_2 V \\ \vdots \\ \rho_N V \\ \rho u V + \eta_x p \\ \rho v V + \eta_y p \\ V(e+p) \end{bmatrix}$$

$$\boldsymbol{H} = \frac{1}{y}\begin{bmatrix} \rho_1 v \\ \rho_2 v \\ \vdots \\ \rho_N v \\ \rho u v \\ \rho v^2 \\ (e+p)v \end{bmatrix}, \quad \boldsymbol{W} = \begin{bmatrix} w_1 \\ w_2 \\ \vdots \\ w_N \\ 0 \\ 0 \\ 0 \end{bmatrix}, \quad \boldsymbol{F}_v = \frac{1}{JRa}\begin{bmatrix} -\rho_1 U_1^d \\ -\rho_2 U_2^d \\ \vdots \\ -\rho_N U_N^d \\ \xi_x \tau_{xx} + \xi_y \tau_{xy} \\ \xi_x \tau_{xy} + \xi_y \tau_{yy} \\ \xi_x \beta_x + \xi_y \beta_y \end{bmatrix}$$

$$\boldsymbol{G}_v = \frac{1}{JRa}\begin{bmatrix} -\rho_1 V_1^d \\ -\rho_2 V_2^d \\ \vdots \\ -\rho_N V_N^d \\ \eta_x \tau_{xx} + \eta_y \tau_{xy} \\ \eta_x \tau_{xy} + \eta_y \tau_{yy} \\ \eta_x \beta_x + \eta_y \beta_y \end{bmatrix}, \quad \boldsymbol{H}_v = \frac{1}{yRa}\begin{bmatrix} -\rho_1 v_1^d \\ -\rho_2 v_2^d \\ \vdots \\ \rho_N v_N^d \\ \tau_{xy} \\ \tau_{yy} - \tau_{\theta\theta} \\ \beta_y \end{bmatrix} \tag{2}$$

Presented as Paper 97-0915 at the AIAA 35th Aerospace Sciences Meeting, Reno, NV, Jan. 6–9, 1997; received April 25, 1997; revision received Jan. 22, 1998; accepted for publication Jan. 25, 1998.

*Postdoctoral Research Associate, Department of Aerospace Engineering. Member AIAA.

†Professor, Department of Aerospace Engineering. Senior Member AIAA.

‡Assistant Professor, Department of Aerospace Engineering. Member AIAA.

where total density ρ is expressed as the sum of the partial density ρ_k of each species:

$$\rho = \sum_{k=1}^{N} \rho_k$$

u and v are velocity components in Cartesian coordinates (x, y), and total energy per unit volume e is defined as the sum of kinetic energy and internal energy. U and V are the contravariant velocity components in generalized coordinates. Coordinate transformation metrics ξ_x, ξ_y, η_x, and η_y and metric Jacobian J are obtained from a coordinate transform relation. Pressure p is evaluated from the ideal gas law for a mixture of thermally perfect gases:

$$\rho = \sum_{k=1}^{N} \frac{\rho_k}{M_k} \boldsymbol{R} T \tag{3}$$

where M_k is the molecular weight for the kth species and $\boldsymbol{R}$ is the universal gas constant. M_k and other molar properties are obtained from Strehlow[21] for the evaluation of transport properties. Temperature T is evaluated implicitly by the Newton–Raphson iteration method with the definition of total energy and the specific heats of each species, which are obtained as function of temperatures from NASA thermochemical polynomial data that are valid up to the temperature of 6000 K (Ref. 22). Although the ideal gas law may introduce some errors at high-temperature and pressure conditions,[23] it is not considered to change the overall flow structures significantly.[6,24]

Although a multicomponent diffusion equation should be used for the evaluation of diffusion velocity components of u_k^d and v_k^d, Fick's law is be used for convenience.[25] Binary mass diffusivity is obtained using the Chapman–Enskog theory in conjunction with Lennard–Jones intermolecular potential functions.[25] Contravariant diffusion velocity components of U_k^d and V_k^d are defined similarly to contravariant velocities in generalized coordinates. Ra in viscous terms are the Reynolds number based on inflow sonic velocity. By applying Stokes' hypothesis, viscous momentum and heat flux terms are reconstructed in generalized coordinates by the chain rule. The laminar values of dynamic viscosity and thermal conductivity of each species are determined by fourth-order polynomials of temperature, which are valid up to a temperature of 6000 K (Ref. 26). Once the viscosity and the conductivity of each species has been determined, the conductivity and the viscosity of the mixture are calculated using Wilke's mixing rule.[25]

Chemistry and Turbulence Modeling

Reaction source term w_k in Eq. (2) is the mass production rate of kth species by N_r chemical reaction steps:

$$w_k = M_k \sum_{r=1}^{N_r} (\nu''_{k,r} - \nu'_{k,r}) \left[k_{fr} \prod_{k=1}^{N} \left(\frac{\rho_k}{M_k} \right)^{\nu'_{k,r}} - k_{br} \prod_{k=1}^{N} \left(\frac{\rho_k}{M_k} \right)^{\nu''_{k,r}} \right] \tag{4}$$

The stoichiometric coefficients $\nu'_{k,r}$ and $\nu''_{k,r}$ are supplied by the hydrogen–air combustion model proposed by Moretti[27] that consists of six reacting species, H, H_2, O, O_2, OH, and H_2O, and one inert species, N_2, with eight significant reaction steps. The forward and backward reaction rate constants k_{fr} and k_{br} for rth reaction step are expressed in Arrhenius form, $k_r = A_r T^{B_r} \exp(-E_r^*/T)$. The reaction coefficients A_r and B_r and activation temperature E_r^* are taken from Evans and Schexnayder.[28] This combustion model is a reduced reaction mechanism that has been successfully used and validated in a number of supersonic reacting flow studies.[11,15,16,29,30] Although this mechanism has not predicted the induction distance accurately in some cases, and there are more accurate models for hydrogen/air combustion,[31] this model is chosen mainly for computational simplicity and efficiency because the more accurate combustion mechanism including more species and pressure-dependent reactions requires a severe increase of computational time, which makes the modeling much more complicated.

As the Reynolds number in a ram accelerator is very high, a fully turbulent flow can be assumed. In the present study, turbulence eddy viscosity is calculated by the Baldwin–Lomax algebraic turbulence model.[32] This model is chosen for its simplicity and the lack of a sufficiently accurate model for this kind of flow. The mixture viscosity and thermal conductivity, as well as the binary diffusivity of the species in the gas mixture, are expressed as sums of the laminar and turbulent values. The constant turbulent Prandtl and Schmidt numbers of 0.9 are assumed to evaluate turbulent thermal conductivity and mass diffusivity. The combustion process in a scram accelerator is mainly accomplished by the oblique detonation, and the major viscous effects are observed at the burned gas region in which the chemical reaction is already completed. Therefore, the interactions between turbulence and chemistry are not considered in the present study because its analysis requires the direct numerical simulation or the closure of reaction source term using the probability density functions, which are not yet applicable to this kind of complex flow.[33]

Numerical Methods

Spatial Discretization

The finite volume cell-vertex scheme is used for spatial discretization of governing equations. The viscous terms are expressed by a central difference method and the convective terms are expressed as differences of numerical fluxes at cell interface:

$$\left(\frac{\partial \boldsymbol{Q}}{\partial t} \right)_{i,j} = \boldsymbol{RES}_{i,j}$$

$$\begin{aligned} \boldsymbol{RES}_{i,j} = {} & -J_{i,j} \left(\tilde{\boldsymbol{F}}_{i+\frac{1}{2},j} - \tilde{\boldsymbol{F}}_{i-\frac{1}{2},j} + \tilde{\boldsymbol{G}}_{i,j+\frac{1}{2}} - \tilde{\boldsymbol{G}}_{i,j-\frac{1}{2}} \right) - \boldsymbol{H}_{i,j} \\ & + \boldsymbol{W}_{i,j} + \frac{\boldsymbol{J}_{i,j}}{2} (\boldsymbol{F}_{vi+1,j} - \boldsymbol{F}_{vi-1,j} + \boldsymbol{G}_{vi,j+1} - \boldsymbol{G}_{vi,j-1}) + \boldsymbol{H}_{vi,j} \end{aligned} \tag{5}$$

The numerical fluxes containing artificial dissipation are formulated using Roe's flux difference splitting (FDS)[34] method. The complete formulation of Roe's FDS method for multispecies chemically reacting flow is based on the method of Grossman and Cinnella[35] extended to two-dimensional curvilinear coordinates[36]:

$$\tilde{\boldsymbol{F}}_{i+\frac{1}{2},j} = \tfrac{1}{2}[\boldsymbol{F}(\boldsymbol{Q}_R) + \boldsymbol{F}(\boldsymbol{Q}_L) - |\boldsymbol{A}(\boldsymbol{Q}_R, \boldsymbol{Q}_L)|(\boldsymbol{Q}_R - \boldsymbol{Q}_L)] \tag{6}$$

where subscripts L and R are the extrapolated values at the left and right grid point of the cell interface $(i + \frac{1}{2})$. $\boldsymbol{A}(\boldsymbol{Q}_R, \boldsymbol{Q}_L)$ implies that the Jacobian matrix $\boldsymbol{A}$ is evaluated by Roe's average of $\boldsymbol{Q}_R$ and $\boldsymbol{Q}_L$. To obtain the appropriate Roe's average for chemically reacting flow, Grossman and Cinnella[35] used the same primitive variable approach as Roe. The artificial dissipation term in Eq. (6) for chemically reacting flow can be written in two-dimensional curvilinear coordinates:

$$\begin{aligned} |\boldsymbol{A}(\hat{\boldsymbol{Q}})|\Delta \boldsymbol{Q} = \boldsymbol{R}|\Lambda|\boldsymbol{R}^{-1}\Delta \boldsymbol{Q} = |\Delta \boldsymbol{F}| = |\Delta \boldsymbol{F}|_1 + |\Delta \boldsymbol{F}|_2 \\ + |\Delta \boldsymbol{F}|_3 + |\Delta \boldsymbol{F}|_4 \end{aligned} \tag{7}$$

where

$$|\Delta \boldsymbol{F}|_1 = \delta w_1 \begin{bmatrix} \hat{y}_1 \\ \vdots \\ \hat{y}_N \\ \hat{u} \\ \hat{v} \\ \hat{H} - (\hat{a}^2/\hat{p}_e) \end{bmatrix}$$

$$|\Delta \boldsymbol{F}|_2 = \delta w_2 \begin{bmatrix} \delta y_1 \\ \vdots \\ \delta y_N \\ \delta u - \xi_x \delta U \\ \delta v - \xi_y \delta V \\ (\xi_x \delta v - \xi_y \delta u)(\xi_x \hat{v} - \xi_y \hat{u}) \\ -\dfrac{1}{\hat{p}_e} \displaystyle\sum_{k=1}^{N} p_{\rho_k} \delta_{y_k} \end{bmatrix} \tag{8}$$

$$|\Delta \boldsymbol{F}|_{3,4} = \delta w_{3,4} \begin{bmatrix} \hat{y}_1 \\ \vdots \\ \hat{y}_N \\ \hat{u} \pm \xi_x \hat{a} \\ \hat{v} \pm \xi_y \hat{a} \\ \hat{H} \pm \hat{a}\hat{U} \end{bmatrix}$$

$$\delta w_1 = \frac{|\nabla\xi|}{J}\psi(\lambda_1)\left(\delta\rho - \frac{\delta p}{\hat{a}^2}\right), \qquad \delta w_2 = \frac{|\nabla\xi|}{J}\psi(\lambda_1)\hat{\rho}$$
$$\delta w_{3,4} = \frac{|\nabla\xi|}{J}\psi(\lambda_{2,3})\left(\frac{\delta p \pm \hat{\rho}\hat{a}\delta U}{2\hat{a}^2}\right) \tag{9}$$

where the caret indicates Roe's averaged value at the cell interface. $\Delta(\,)$ and $\delta(\,)$ are the difference of the extrapolated values at the left and right grid points, respectively. Grid metrics of ξ_x and ξ_y are used after normalization. H $(=(e + p)/\rho)$ is enthalpy per unit mass, and frozen sonic velocity is derived from the definition of the eigenvalue, which can be rewritten in compact form by introducing the definition of frozen specific heat ratio:

$$a^2 = \bar{\gamma}\frac{p}{\rho}, \qquad \bar{\gamma} = \frac{\sum_{k=1}^{N}\rho_k c_{p_k}}{\sum_{k=1}^{N}\rho_k c_{v_k}} \tag{10}$$

Pressure derivatives p_e and p_{ρ_k} are derived from the ideal gas law:

$$p_e = \bar{\gamma} - 1, \qquad p_{\rho_k} = \frac{\bar{\gamma}\boldsymbol{R}\boldsymbol{T}}{\boldsymbol{M}_k} + p_e\left[\frac{1}{2}(u^2 + v^2) - \int^T c_{p_k}\,\mathrm{d}T + h_k^0\right] \tag{11}$$

Because Roe's FDS method does not satisfy the second law of thermodynamics and sometimes shows unphysical solutions when the eigenvalue is too small, the entropy fixing function by Montagne et al.[37] is used to prevent the problems. In Eq. (9) $\psi(\lambda)$ is the corrected eigenvalue. Because all upwind schemes have monotonicity but first-order spatial accuracy, higher-order extension of the upwind scheme is needed for the postshock solution accuracy. Therefore, the MUSCL[38] scheme is used for the extrapolation of primitive variables at the cell interface. In addition, the minmod limiter function is used to overcome the severe dispersion error introduced by the higher-order extrapolation and to preserve the total variation diminishing property.[38]

Time Integration

The spatially discretized governing equation (5) can be rewritten by a point implicit time integration method as follows:

$$\left[\frac{\boldsymbol{I}}{\Delta t} - \boldsymbol{Z}\right]_{i,j}^{n}\Delta\boldsymbol{Q}_{i,j} = \boldsymbol{RES}_{i,j}^{N}, \qquad \boldsymbol{Q}^{n+1} = \boldsymbol{Q}^n + \Delta\boldsymbol{Q} \tag{12}$$

where $\boldsymbol{Z}$ is the chemical source Jacobian matrix and n is the time integration step. This form of point implicit time integration method is used for the unsteady marching problem. Although this integration method is first-order accurate in time, temporal accuracy can be preserved using a small time step size. This kind of an approach has also been used for the analysis of the periodically unstable shock-induced combustion problem.[17] The matrix inversion process of Eq. (12) can be done efficiently by splitting the Jacobian matrix and the residual vector.[11]

Although the point implicit method is used for the analysis of unsteady reacting flow calculation, the more efficient lower–upper symmetric successive overrelaxation (LU-SSOR)[26] method is used for the computation of the steady frozen flow solution that is used as an initial condition for the unsteady marching process. By applying the LU-SSOR method, governing equations can be integrated fully implicitly by the diagonal lower and upper steps with an approximate Jacobian splitting method[26]:

$$\boldsymbol{D}_{i,j}\Delta\boldsymbol{Q}_{i,j}^{*} = \boldsymbol{RES}_{i,j} + J_{i,j}\left(\boldsymbol{A}_{i-1,j}^{+}\Delta\boldsymbol{Q}_{i-1,j}^{*} + \boldsymbol{B}_{i,j-1}^{+}\Delta\boldsymbol{Q}_{i,j-1}^{*}\right) \tag{13}$$

$$\boldsymbol{D}_{i,j}\left(\Delta\boldsymbol{Q}_{i,j}^{n} - \Delta\boldsymbol{Q}_{i,j}^{*}\right) = -J_{i,j}\left(\boldsymbol{A}_{i+1,j}^{-}\Delta\boldsymbol{Q}_{i+1,j}^{n} + \boldsymbol{B}_{i,j+1}^{-}\Delta\boldsymbol{Q}_{i,j+1}^{n}\right) \tag{14}$$

$$\boldsymbol{D}_{i,j} = \lfloor \boldsymbol{I}/\Delta t + J_{i,j}\{\sigma(\lambda_A) + \sigma(\lambda_B)\}\rfloor_{i,j}$$
$$\sigma(\lambda) = \kappa\cdot(|U| + a|\nabla\xi|), \qquad \kappa \geq 1 \tag{15}$$

$$\boldsymbol{A}^{\pm}\Delta\boldsymbol{Q} = \frac{1}{2}[\boldsymbol{A} \pm \sigma(\lambda)]\Delta\boldsymbol{Q} = \frac{|\nabla\xi|}{2J}\begin{bmatrix} y_1 A + B\delta q_1 \\ \vdots \\ y_N A + B\delta q_N \\ uA + B\delta q_{N1} + \xi_x C \\ vA + B\delta q_{N2} + \xi_y C \\ HA + B\delta q_{N3} + UC \end{bmatrix}$$
$$A = \xi_x\delta q_{N1} + \xi_y\delta q_{N2} - U\sum_{k=1}^{N}\delta q_k, \qquad B = U \pm \sigma(\lambda)$$
$$C = \sum_{k=1}^{N} p_{\rho_k}\delta q_k - p_e(u\delta q_{N1} + v\delta q_{N2} - \delta q_{N3}) \tag{16}$$

The matrix-vector products in Eqs. (13) and (14) are burdens of computational work that can be done more efficiently by the formulation in Eq. (16). This formulation saves about 30–40% of total computation time.

The numerical algorithms used in this study were validated through a number of numerical simulations for the cases where experimental data exist, such as the shock-induced combustion phenomena around a blunt body and the shock/boundary-layer interaction problems. The locations of shock wave and reaction front are compared for the former problem, and the wall pressure and skin-friction coefficient distributions are compared for the latter problem. Comparison of the numerical result with the experimental data showed acceptable agreement and the detailed descriptions about the validation works can be found in Refs. 19, 20, and 30.

Computational Domain and Space Marching

An experiment of superdetonative launching process was done by the Institute of Saint-Louis (ISL)[10] for a configuration similar to that of Fig. 1. The experiment used 30-mm-diam projectiles in a 41-mm-wide rail tube. The projectile has 45–60 mm long combustor section with nose and tail cone angle of 14–16 deg. The mass of projectile is 125–135 g. The launcher part is filled with $2H_2 + O_2 + m CO_2$ mixtures maintained at about 27 atm, where m changes as 3.1, 3.8, 5.1, and 6.8. For these mixtures, the launching velocity of about 1800 m/s is 17–52% in excess of Chapman–Jouguet (C–J) detonation velocities. A sharp velocity decrease (lower dilution limit unstart) was found for the $2H_2 + O_2 + 3.1CO_2$ mixture, and a very small velocity gain (upper dilution limit unstart) was obtained for the $2H_2 + O_2 + 6.8CO_2$ mixture.[10] The maximum velocity gain of about 200 m/s is obtained for $2H_2 + O_2 + 3.8CO_2$ in the 3.6-m-long rail tube.

To simulate the injection process of a scram accelerator projectile from air into a high-pressure mixture, the scram accelerator configuration in Fig. 1 is considered. It is composed of a projectile and a barrel that is divided into a launcher and an accelerator part by a diaphragm. The projectile body is 22 cm in length and 2.8 cm in diameter. The barrel is 4.0 cm in diameter. The nose and tail of the projectile are symmetric with a half-angle of 10 deg. The projectile mass of 150 g is assumed. The launcher part is filled with 1 atm air and the accelerator part is filled with $2H_2 + O_2 + mN_2$ mixtures maintained at 25 atm and 300 K, where dilution ratio m varies from 3.76 to 9. Although CO_2 was used as a diluent gas in the experiment of ISL, N_2 is selected and assumed to be inert for computational efficiency because a nitrogen mixture requires a small number of species and reaction steps. Initial velocity of 2500 m/s is assumed, and a steady-state solution is obtained for the launcher part air condition, which is used as an initial condition for the transient

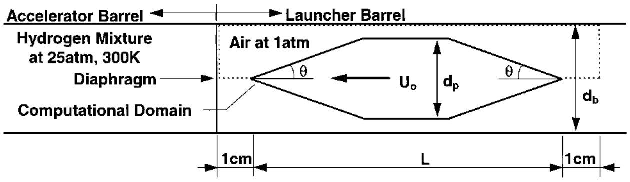

Fig. 1 Configuration of scram accelerator at starting position: U_o = 2500 m/s, L = 22 cm, d_p = 2.8 cm, d_b = 4.0 cm, and θ = 10 deg; mass of the projectile is assumed as 150 g.

Table 1 Summary of sonic velocity a, Mach number M, C–J detonation wave velocity V_{det}, and overdrive factor $f_{overdrive}$ (initial projectile velocity/C–J detonation wave velocity, V_p/V_{det}) for various mixtures at initial launching state

Mixture	a, m/s	M	V_{det}, m/s	$f_{overdrive}$
Air	352.75	7.19	——	——
$2H_2 + O_2 + 3.76N_2$	409.68	6.10	2,053	1.22
$2H_2 + O_2 + 4.5N_2$	402.84	6.21	1,973	1.27
$2H_2 + O_2 + 5N_2$	399.09	6.26	1,925	1.30
$2H_2 + O_2 + 6N_2$	393.05	6.36	1,838	1.36
$2H_2 + O_2 + 7N_2$	388.41	6.43	1,763	1.42
$2H_2 + O_2 + 8N_2$	384.73	6.50	1,697	1.47
$2H_2 + O_2 + 9N_2$	381.73	6.55	1,641	1.52

simulation. This steady-state condition corresponds to the inflow Mach number of 7.19 and Reynolds number of 1.49×10^8/m. The transient simulations of the ram accelerator starting process are performed for the seven cases of mixtures with m ranging from 3.76 to 9. The initial projectile velocity of 2500 m/s is regarded as a reasonable value for the superdetonative operation of a ram accelerator because it is 20–50% in excess of C–J detonation velocities. The C–J velocities for considered mixtures are calculated by using a separate thermodynamics code and are presented in Table 1.

The computational domain is extended by 1 cm before and after the projectile. The no-slip condition is applied at the projectile surface and the barrel wall. The solid surfaces are assumed to be kept at the constant temperature of 600 K as that was assumed by Yungster[16] in a similar ram accelerator study. A symmetric condition is used at the axis of symmetry, and simple extrapolation is used for outflow. The computational domain is covered with 400 uniformly distributed grid points in the axial direction because the unsteady propagation of normal or stiff oblique detonation wave happens there during operation; 60 grid points are used in the radial direction, which are clustered at both walls to ensure the pressure and shear stress distribution. The axial grid spacing $\Delta x/L$ is 0.0027, and the minimum value of y^+ at the points nearest to the wall equals 2.5. Prior to the reacting flow simulation, the solution independency of the grid system was studied for steady nonreacting flow with coarser and finer grids by examining the pressure and shear stress distribution at the projectile surface. In reacting flow simulation, the early stage of the $2H_2 + O_2 + 3.76N_2$ case was examined using finer grids, and essentially the same flow features were found. The $2H_2 + O_2 + 7N_2$ mixture case was also tested with finer grids, and the comparison of the quasisteady wall pressure distributions showed nearly the same magnitude and locations of pressure peaks. Therefore, the 400×60 grid was considered sufficient for capturing the global features of the combustion flowfields.

For the evaluation of the initial condition, the LU-SSOR method and a local time stepping technique is used. For the transient simulations of launching process, the governing equations are temporally integrated by the point-implicit method with minimum time step. In most cases, the time step is set to a constant value of 6.15 ns, which corresponds to the Courant–Friedrichs–Lewy number of 0.5, based on the minimum grid size. At the early stage of transient simulation, the mixture condition is imposed at the computational cells between the inflow boundary and the diaphragm. In the body-fixed coordinate, the diaphragm is positioned initially at the inflow boundary that is located 1 cm ahead of the projectile nose. The diaphragm is artificially moved at the projectile velocity, and it is assumed to break down suddenly when it reaches the projectile nose. The projectile marches with the velocity variation until it advances a sufficient distance.

During calculation, the projectile velocity is considered to be changed by the thrust force exerted by flowfield. At any instance, the velocity variation ΔV_p of the projectile is determined as

$$\Delta V_p = a_p \Delta t \tag{17}$$

The force acting on the body is evaluated by integrating the pressure and the wall shear stress over the projectile surface, and the acceleration of the projectile a_p is obtained from the force divided by the projectile mass. The projectile velocity V_p is determined by adding the velocity variation to the previous value, and the velocity variation is imposed on all of the computational grid points to consider the variations of the local values of axial velocity and the total energy:

$$V_p^{n+1} = V_p^n + \Delta V_p, \qquad \tilde{u}_{i,j}^n = u_{i,j}^n + \Delta V_p \tag{18}$$

$$\begin{aligned} e_{i,j}^{n+1} &= e_{i,j}^n - \tfrac{1}{2}(\rho u^2)_{i,j}^n + \tfrac{1}{2}(\rho \tilde{u}^2)_{i,j}^n \\ &= e_{i,j}^n + \tfrac{1}{2}\rho_{i,j}^n\left(2u_{i,j}^n + \Delta V_p\right)\Delta V_p \end{aligned} \tag{19}$$

As the one-dimensional motion of the projectile is considered, the described procedure is equivalent to consideration of one-dimensional grid motion in a moving reference frame. Although this procedure corresponds to a first-order accurate method, it is used because there is no sufficiently accurate method to include the effect of velocity variation. Also, it is not likely to affect the global time accuracy because the velocity increment is confined to a very small value at every time step.

The performance of the ram accelerator may be expressed by thrust coefficient (TC) and ballistic efficiency η_b (Ref. 15). TC is defined here as the ratio of the thrust acting on the body and the initial pressure on the projectile cross section. The ballistic efficiency is the ratio of the increase of kinetic energy to the heat release rate. The heat release rate is defined as the difference of heat flux at the inlet and at the exit.

Results

To understand of the ignition and the detonation initiation characteristics involved in the injection process from the launcher barrel to the accelerator barrel, numerical simulations are performed for the mixtures ranging from $2H_2 + O_2 + 3.76N_2$ to $2H_2 + O_2 + 9N_2$. For all of the cases, the combustion process develops in a similar way, except for the limit cases, and positive acceleration is achieved even though the process does not occur at same time or in same sequence. Thus, only the three unsteady results are discussed in the marching sequence, and the other cases are compared at the final stage. In the following results, the upper parts of Figs. 2–4 are the temperature distributions, in Kelvin, and the lower parts are the pressure distributions, in standard atmospheric pressure, unless otherwise specified. The spatial position denoted by x_p is the projectile flight distance from the diaphragm. Figures 2–5 are magnified by a factor of two in the vertical direction for clarity. Therefore, all of the wave angles in the plots are exaggerated.

Case of $2H_2 + O_2 + 3.76\,N_2$ Mixture

Figure 2 is the result for $2H_2 + O_2 + 3.76N_2$, which is most reactive and energetic among the mixtures considered. For this mixture, the initial Mach number is 6.1 and the overdrive factor is 1.22. At $x_p = -0.5$ cm, the diaphragm is marked as a stiff pressure gradient in front of the projectile nose. As the projectile marches only 0.5 cm from the initial state, the result is nearly same as that of steady state. A thin thermal boundary layer is formed on the body surface, and a high-temperature and high-pressure region exists at the shock wave impinging point on the middle of the body surface.

Just after the breakdown of the diaphragm ($x_p = 2.0$ cm), a normal shock system develops and moves downstream. A bubble of detonation appears at the projectile nose after the passage of the normal shock system. Then, the bubble of detonation grows very rapidly in the radial and downstream directions. Finally, the detonation catches up with the nonreacting normal shock, although it cannot expand upstream because the projectile velocity is 22% higher than that of C–J detonation velocity. At this stage, the high-drag force (reverse thrust force) begins to act on the body due to the high-pressure region inside the bubble even though the drag force is limited to a small value because it acts only on the nose tip of the body. This spontaneous ignition may be due to the interaction between the normal shock system (a normal shock followed by a contact surface and expansion waves) and the oblique shock wave, as discussed in previous work.[20]

As the bubble of detonation expands ($x_p = 7.0$ cm), a bow shock is reflected on the barrel wall and the reflection procedure is repeated

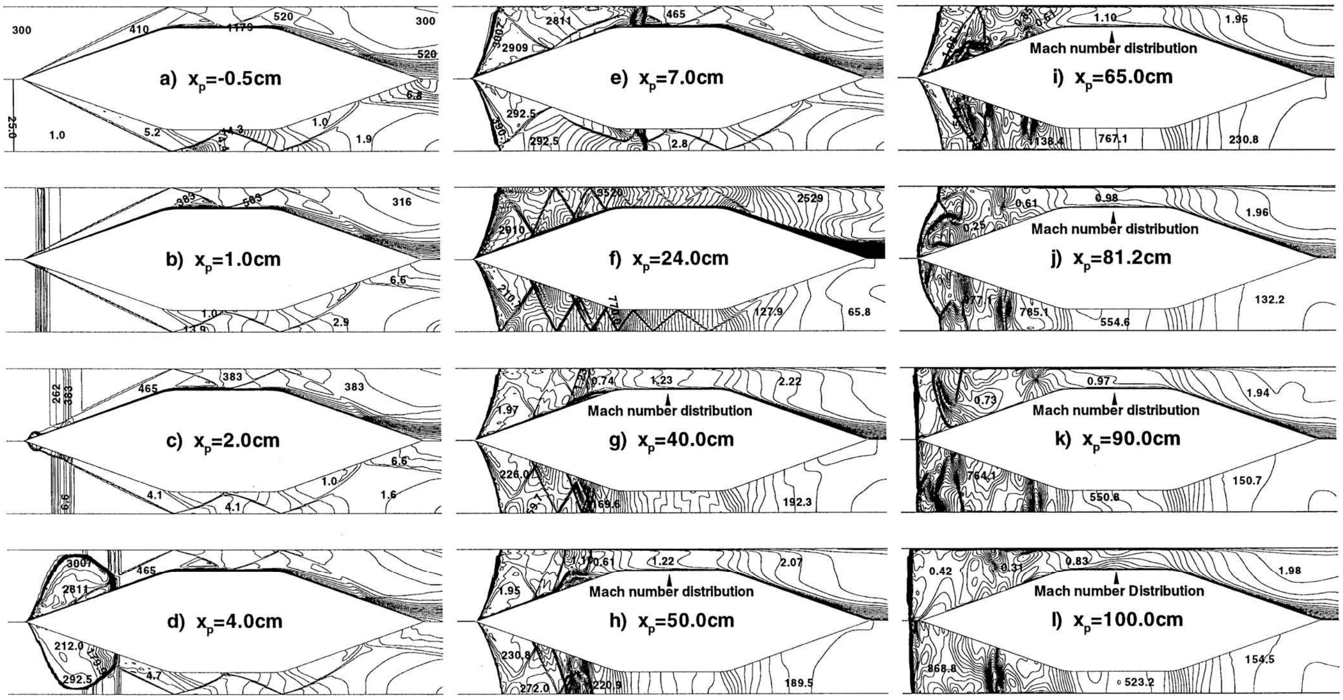

Fig. 2 Temperature distributions (upper half of each figure) and pressure distributions (lower half of each figure) in marching sequence for $2H_2 + O_2 + 3.76N_2$ mixture; Mach number distributions are plotted for cases after x_p = 40.0 cm.

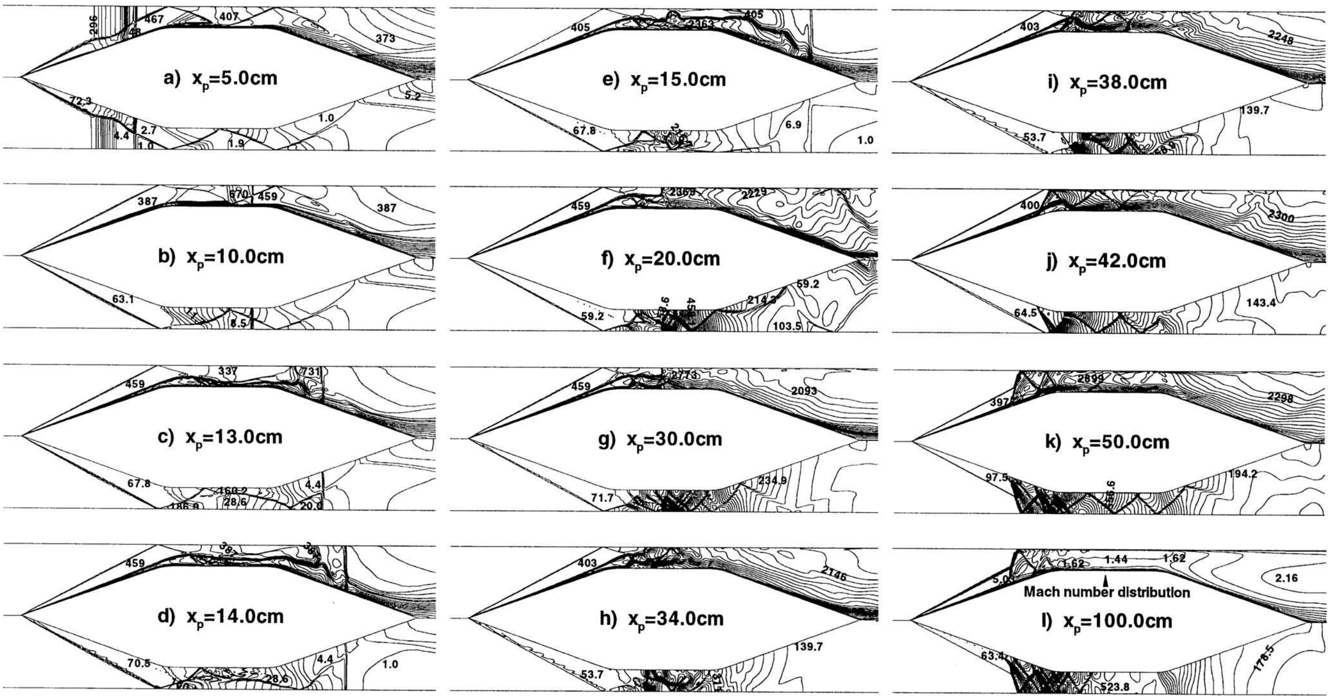

Fig. 3 Temperature distributions (upper half of each figure) and pressure distributions (lower half of each figure) in marching sequence for $2H_2 + O_2 + 5N_2$ mixture; Mach number distribution is plotted for case of x_p = 100.0 cm.

on the body surface. After the aforementioned shock–shock interaction, the preceding normal shock is left as a following contact surface while the normal detonation moves downstream. A drag force increases enormously, and the projectile velocity begins to drop sharply because the high-pressure burned gas occupies all of the frontal area of the body. Hereafter, the shock reflection procedure is repeated several times until the regular pattern of the shock train is formed ($x_p = 24$ cm). During this shock-train forming period, the acceleration is maintained at about the value of $-15{,}000\,g$ (refer to Fig. 6) for a sufficiently long time, although the acceleration shows an oscillatory behavior because of the variation of the shock-impinging points on the conical nose and tail. The slope of the oblique shock in the burned gas region is much steeper than that in the airflow because the flow Mach number is low due to the high sonic velocity in this region, even though the flow velocity is kept in the same order of magnitude.

On the other hand, strong shock wave/boundary-layer interactions are observed at the three shock-impinging points on the conical nose. This interaction is strongest at the second impinging point and is enough to generate the separation bubble. As time goes on, the severe shock–shock interactions and shock wave/boundary-layer interactions are repeated and form the strong oblique shock ahead of the large separation bubble. As a result, thermal choking is provided by a strong shock at the back of the separation bubble ($x_p = 40$ cm). The oblique shock moves forward continuously and interacts with the incident oblique detonation. The triple-shock interaction point

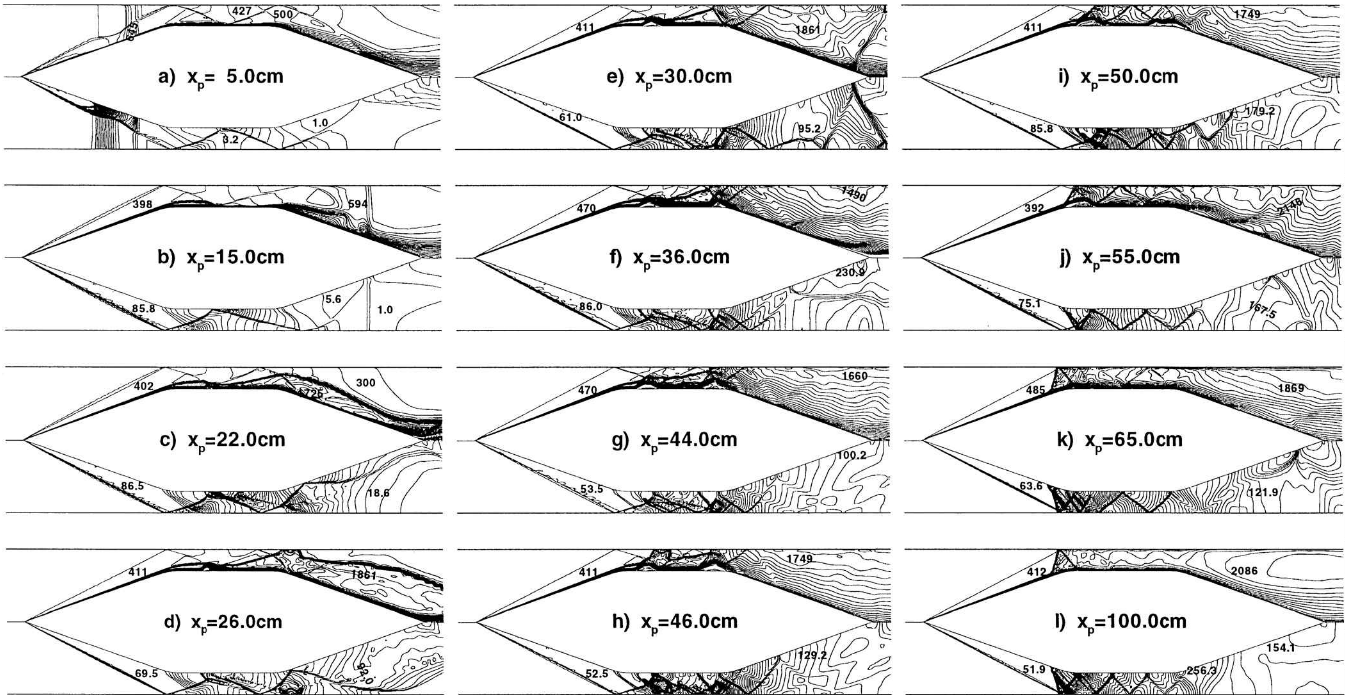

Fig. 4 Temperature distributions (upper half of each figure) and pressure distributions (lower half of each figure) in marching sequence for $2H_2 + O_2 + 7N_2$ mixture.

is shown when the projectile marches 81.2 cm. Finally, a normal detonation is formed ahead of the projectile and propagates upstream with the support of thermal choking. This unstart behavior coincides with the experimental result observed by Seiler et al.,[10] although the flow conditions are different. The acceleration of $-30{,}000\,g$ is nearly same as the experimental results.

Case of $2H_2 + O_2 + 5N_2$ Mixture

Figure 3 is the result for the $2H_2 + O_2 + 5N_2$ mixture. At 5-cm movement after the diaphragm breakdown, the interaction between an oblique shock and a normal shock system is clearly shown. As the projectile moves 10 cm, the normal shock system passes the shock wave/boundary-layer interaction region, and the ignition occurs in the boundary layer, as previously shown by Yungster.[16] After this stage, the low-pressure burned gas generated in the boundary layer expands downstream while the normal shock passes through the projectile tail. A shock-induced combustion is initiated weakly behind the normal shock but is merged with the expanding boundary layer. During this process, the edge of the boundary layer is represented by a temperature gradient where the reaction progresses. The expanding burned gas boundary acts as a strong contact surface across which the temperature and the density vary severely but the pressure changes negligibly.

The reflected shock from the barrel wall deflects with a larger angle when it crosses the expanding burned gas boundary, and this deflection forwards the shock-impinging point. At the body surface, the oblique shock wave rapidly interacts with boundary layer, and the strong shock-impingement forms a new oblique shock, although the mixture downstream of the impinging point burns more quickly than that in the nose boundary layer due to its more compressed condition. A strong oblique shock wave reflection is shown at $x_p = 15$ cm. The reflected oblique shock interacts with the burned gas boundary to form a detonation normal to the barrel wall. Although the reaction front downstream of the previous impinging point expands and pushes up the oblique shock, it no longer exists as a reaction front due to the development of the new detonation front.

This form of interaction is maintained for a long period, which is equivalent to the duration of more than 10 cm, until the separation bubble grows enough to make a strong oblique shock ahead. The growth of the separation bubble is recognized by comparing temperature contours at $x_p = 20$ and 30 cm. In this period, thrust is generated in a regular manner, and the projectile velocity increases linearly. The high-temperature and high-pressure burned gas expands through the conical nozzle and generates the thrust corresponding to more than $5000\,g$ (refer to Fig. 6). The thrust coefficient defined proportional to acceleration showed a peak value of about 9 when the scram accelerator operates in a regular manner.

When the separation bubble is large enough to generate the oblique shock outside the burned gas boundary, the oblique shock is transformed to the oblique detonation and moves forward to the conical nose. Finally, the oblique detonation loads high-pressure force to the conical nose and results in the severe reduction of acceleration of about zero. The oblique detonation settles down at a specific point on the conical nose after a sufficient march. This process occurs during $x_p = 34$–42 cm. At $x_p = 50$ cm, the regular pattern of the shock train is clearly shown, although there still exist strong shock wave/boundary-layer interactions. After $x_p = 50$ cm, the flowfield shows a choked-like behavior, even though choking has not occurred. The acceleration shows an oscillatory behavior resulting in nearly constant velocity. After $x_p = 70$ cm, the flowfield seems to be stabilized without significant change; the flowfield at $x_p = 100$ cm is nearly the same as the result at $x_p = 70$ cm.

Case of $2H_2 + O_2 + 7N_2$ Mixture

Figure 4 is the result for the $2H_2 + O_2 + 7N_2$ mixture. After the breakup of the diaphragm, an interaction between the oblique shock and the normal shock system is shown with the flowfield similar to that of the $2H_2 + O_2 + 5N_2$ mixture. When the projectile moves 15 cm from the diaphragm, ignition occurs in the boundary layer downstream of the front and rear expansion corners. The mixture downstream of the impinging point burns quickly because of its more compressed condition and forms a main reaction front behind a reflected shock although the low-pressure burned gas generated in the front boundary layer expands downstream ($x_p = 22$ cm). However, combustion develops more slowly than the $2H_2 + O_2 + 5N_2$ mixture because this mixture is less reactive and less energetic than that mixture.

As the projectile moves forward, oblique shock-induced combustion develops rapidly in the rear part of the projectile. The upstream preburned boundary layer does not expand rapidly as it does in the $2H_2 + O_2 + 5N_2$ mixture. The shock-induced combustion front expands gradually and reflects at the barrel wall. As the projectile marches farther ($x_p = 30$ cm), the reflected reaction front interacts with the reflected shock and forms a detonation front to the barrel

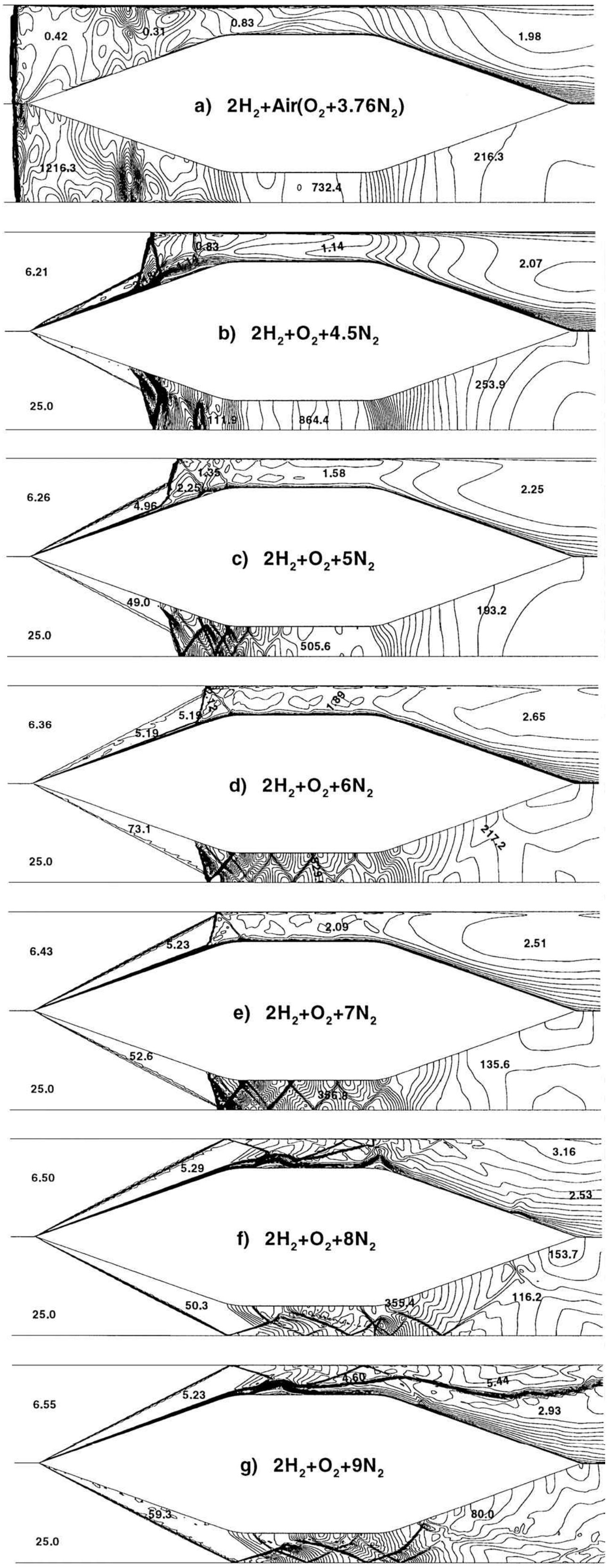

Fig. 5 Mach number distributions (upper half of each figure) and pressure distributions (lower half of each figure) for $2H_2 + O_2 + m\,N_2$ mixtures varying m from 3.76 to 9.

Table 2 Summary of computational result at projectile flight distance of 100 cm, where D_v is viscous drag acting on projectile body

Mixture	ΔV_p, m/s	a_p, g	TC	D_v/F	η_b,%
$2H_2 + O_2 + 3.76N_2$	−84.90	−34,494	−28.44	8.34×10^{-5}	——
$2H_2 + O_2 + 4.5N_2$	−15.72	−10,739	−10.50	9.09×10^{-4}	——
$2H_2 + O_2 + 5N_2$	9.96	4,230	3.99	-3.51×10^{-3}	8.47
$2H_2 + O_2 + 6N_2$	17.84	6,662	6.29	-2.30×10^{-3}	14.50
$2H_2 + O_2 + 7N_2$	17.84	6,493	6.50	-2.31×10^{-3}	16.22
$2H_2 + O_2 + 8N_2$	18.33	8,090	7.62	-1.50×10^{-3}	21.44
$2H_2 + O_2 + 9N_2$	0.80	500	0.47	-2.81×10^{-2}	4.90

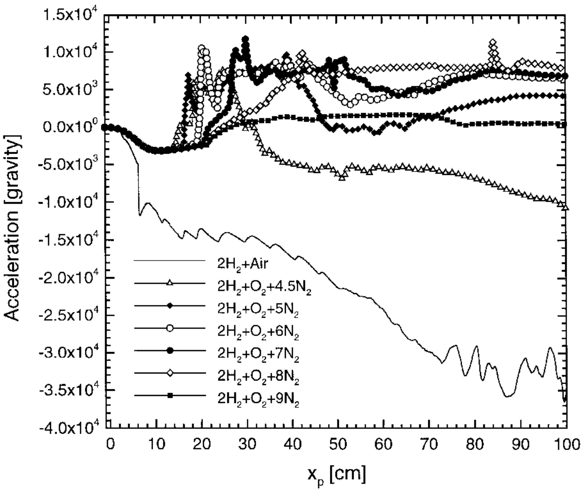

Fig. 6 Variation of acceleration for different mixtures with respect to projectile flight distance from diaphragm.

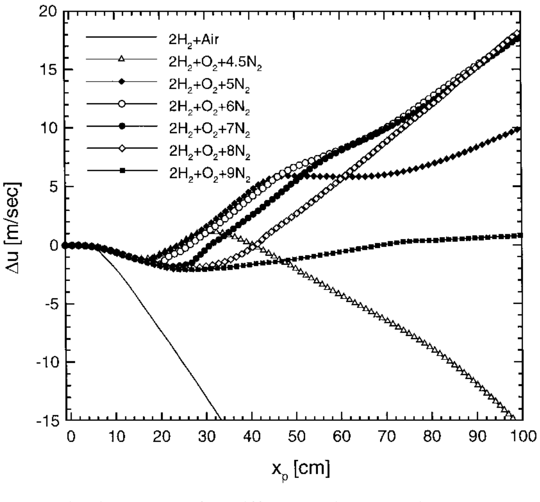

Fig. 7 Velocity increment for different mixtures with respect to projectile flight distance from diaphragm.

wall. After the interaction between the oblique shock and reaction front, a deflected shock heats the projectile surface. A strong shock reflection and a separation bubble is shown around the rear expansion corner. The reflection increases the thrust force enormously to about 10,000 g (refer to Fig. 6).

In the meanwhile, the shock impingement on the middle of the body leads to the gradual growth of the separation bubble that induces a leading oblique shock ahead of it. As time goes on ($x_p =$ 44 cm), the separation bubble is getting larger and the leading oblique shock is getting stronger. Finally at $x_p = 46$ cm, the oblique shock is transformed to a new oblique detonation and the old reaction front disappears. The new oblique detonation moves forward with the support of the separation bubble and settles down on the conical ramp. This movement of oblique detonation results in a reduction of thrust as in the $2H_2 + O_2 + 5N_2$ mixture. After projectile moves more than 65 cm, the flowfield seems to be stabilized and shows a quasisteady (near steady) solution. At the final stage, the projectile acceleration is about 6500 g and the velocity gain of about 18 m/s is attained.

Comparison of Flowfield at 100-Centimeter Projectile Flight Distance

The flowfield results for different mixtures are plotted in Fig. 5 after 100-cm flight. The variations of acceleration and velocity are plotted in Figs. 6 and 7, and the performance parameters at the final stage are summarized in Table 2. Although the case of the

$2H_2 + O_2 + 3.76N_2$ mixture is in a superdetonative mode, a normal detonation is formed and propagates upstream because the thermal choking condition is provided. The sharp decrement of the projectile velocity is comparable to the experimental unstart result,[10] even though the present simulation corresponds to the earlier stage of the experiment. The final value of acceleration is about $-30{,}000\,g$, which is comparable to the experimental result. Therefore, the experimentally investigated lower dilution limit unstart phenomena[10] might be result of the formation of oblique detonation wave at the nose and the thermal choking condition provided there by the strong shock wave/boundary-layer interaction.

The combustion process in a $2H_2 + O_2 + 4.5N_2$ mixture shows a faster but very similar trend to the $2H_2 + O_2 + 5N_2$ mixture. However, the postdetonation flow is thermally choked at the final stage, and oblique detonation is stabilized at the front position of the nose cone. Therefore, the ram accelerator unstarts, and velocity decreases severely at the final stage even though the velocity increases at the ignition period. From the velocity and acceleration curve, it is observed that the oblique detonation moves forward at the earlier stage. The acceleration is about $-10{,}000\,g$ and velocity decreases about 16 m/s at the final stage. Although it has not been found in the experiment at ISL, this result is considered as a lower dilution limit unstart that can be present at a critical mixture condition.

In the $2H_2 + O_2 + 5N_2$, $2H_2 + O_2 + 6N_2$, and $2H_2 + O_2 + 7N_2$ mixtures, the stabilized oblique detonation is observed at the nose. For all these cases, the flowfields are considered to be stabilized at the final stage, but thermal choking is not observed. Thus, the flow velocity is maintained at a supersonic speed, and all of these cases exhibit regular acceleration although the magnitude of the acceleration is different. Distinguished features observed for these mixtures are that the oblique detonation wave stabilization point moves downstream as the mixture gas is diluted and the projectile velocity does not decrease in the less energetic mixture. Actually, the less energetic the mixture is, the larger the thrust is. This result is because the position of oblique detonation is important in view of the force balance along the axisymmetric projectile surface because the postdetonation pressure is high enough to cause a severe reduction of thrust.

The final situation of the $2H_2 + O_2 + 8N_2$ mixture is very similar to the result at $x_p = 36$ cm in $2H_2 + O_2 + 7N_2$. A decoupled oblique shock-induced combustion is observed at the midsection of the projectile, and an intersected normal detonation is formed to the barrel wall. As the heat release in $2H_2 + O_2 + 8N_2$ mixture is not enough to grow the separation bubble, the oblique detonation induced by the separation bubble is not noticed. The oblique shock-induced combustion and the normal detonation are preserved as a main reaction front until the end of the calculation. As the oblique detonation is not formed on the conical ramp, the velocity increases continuously, and the acceleration shows the highest value among the cases considered. The final velocity gain is about 18 m/s and the acceleration is about $8000\,g$. Even though this velocity gain is not very significant, it is conceived as a reasonable value, in comparison with the result at ISL,[10] if we consider the actual distance of positive acceleration. Thrust coefficient and ballistic efficiency also showed maximum values of 7.62 and 21.44%, respectively. Thus, among the cases considered in this study, the reacting flowfield configuration in the $2H_2 + O_2 + 8N_2$ mixture is shown as optimum for maximum performance because the main combustion region is maintained at the midsection of the ram accelerator projectile. However, this kind of solution is rarely attained and is considered as a critical result because the protrusion of the oblique detonation develops for the more energetic mixture and the upper dilution limit unstart occurs at for the less energetic mixture, as discussed in the following.

In the more diluted $2H_2 + O_2 + 9N_2$ mixture, the velocity increase and the acceleration show the values of nearly zero because the heat release is not enough to generate a thrust force. The major difference of combustion flowfield to that of $2H_2 + O_2 + 8N_2$ is that the reaction front could not expand enough to be reflected at the barrel wall. Thus, most of the high-density unburned mixture flows through the narrow region between the barrel wall and reaction front. Because combustion is not fully accomplished and most of the mixture flows in an unburned state, the pressure rise is limited to a small value and to ram accelerator unstart. Although the acceleration shows a slightly positive value, this result is considered as the upper dilution limit unstart, which is observed experimentally, because the sufficient increment of the velocity cannot be expected for this case.

Viscous Effect and the Stabilization of Oblique Detonation Wave

As already mentioned the viscous effect plays a very important role in a scram accelerator operation because the viscous effect induces complex flow interactions even though the viscous drag is negligible, as shown in Table 2. In a regular operating condition, the ignition of the mixture initiates at the shock wave/boundary-layer interaction point, where the temperature is very high due to the aerodynamic heating, as shown in the previous study of superdetonative[16] and transdetonative mode[6] operation. Figure 8 is the stabilized flowfield for the $2H_2 + O_2 + 8N_2$ mixture at the final stage. The main combustion front is composed of the oblique shock-induced combustion behind the reattachment shock and the normal detonation to the barrel wall. A large separation bubble is shown at the shock-impinging region at the projectile surface and the separation bubble induces a strong oblique shock ahead of it. A similar result of the large separated flow region is also found from the experimental OH planer laser-induced fluorescence image of Morris et al.[39] and its numerical simulation.[40] In the burned gas boundary layer of more energetic mixtures, the growing process of the separation bubble has a very close relation with the ram accelerator performance. The oblique shock ahead of the separation bubble can be changed into a new oblique detonation that reduces thrust by settling down on the conical nose. Sometimes the large separation bubble blocks most of the combustor section and causes the thermal choking that results in the lower dilution limit unstart.

After the burning of the mixture, local temperature increases whereas local density decreases. Therefore, the local values of sonic velocity and viscosity of burned gas increase. Because of this, local values of Mach number and Reynolds number are maintained at order of 2 and 1×10^6, respectively, which are considered small values in comparison with the values for the nonreacting flow. Thus, the effect of viscosity is shown to be more enhanced than that in the nonreacting flow. Such a strong viscosity effect influences not only the regular ignition or initiation process but also the stabilization of oblique detonation at the final stage.

Previously, Yungster[16] showed the initiation of coupled shock and combustion wave in a ram accelerator and discussed the mechanism

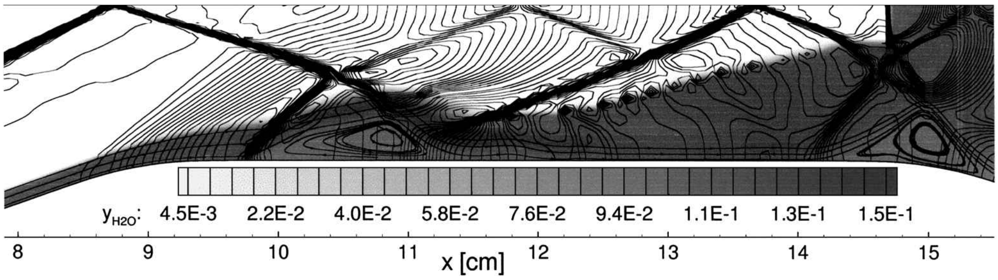

Fig. 8 Magnified view of internal combustion flowfield for case of $2H_2 + O_2 + 8N_2$ mixture; overlaid plot of the distribution of H_2O mass fraction, pressure contours, and streamlines in boundary layer.

of the stiff wave angle. For the investigation of the stabilized structure of oblique detonation, Li et al. have conducted numerical research with an inviscid Euler equation, and the basic structure of stabilized oblique detonation can be understood from their work.[14] However, the stabilized structure of oblique detonation seems to have been described only for a simple configuration, and the detailed description of the interaction between the oblique detonation wave with the separation bubble is rarely found even in Ref. 41, which includes the effect of boundary layer. Because the present study reveals that the viscous effect is important in the ram-accelerator configuration, a detailed description of the oblique detonation wave structure will be discussed by including the viscous effect.

For the cases considered in this study, the oblique detonation wave is formed at the conical ramp for mixtures from $2H_2 + O_2 + 4.5N_2$ to $2H_2 + O_2 + 7N_2$. In comparison with the results in Fig. 5, it is readily found that the location of the oblique detonation wave moves downstream as the quantity of diluent gas increases. However, the structure of the stabilized oblique detonation waves looks similar, and complex shock trains are shown downstream. To investigate the flow structure closely near the oblique detonation wave, the result of the case of $2H_2 + O_2 + 6N_2$ mixture is plotted in Fig. 9 (with magnification). A separation bubble is shown at the origin of oblique detonation, and compression waves are formed ahead of this separation bubble. The compression waves and the deflagration wave, i.e., an edge of the thermal boundary layer, merge and form an oblique detonation. Meanwhile, expansion waves are present after the oblique detonation wave that was generated around the separation bubble. Recompression waves are found downstream of the separation bubble and form a reattachment shock in the burned gas region. After the collision of incidence shock and the detonation front, a slip line is present downstream, as can be seen by the wiggles of the pressure contours (Fig. 9). Similar flow features are also found in other cases and are summarized as a schematic plot in Fig. 10.

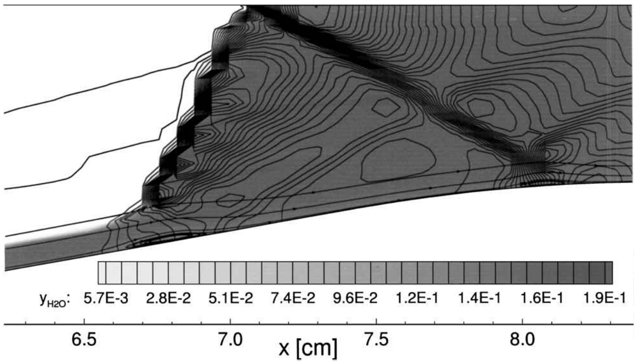

Fig. 9 Magnified view of flowfield near oblique detonation for case of $2H_2 + O_2 + 6N_2$ mixture; overlaid plot of the distribution of H_2O mass fraction, pressure contours, and streamlines in boundary layer.

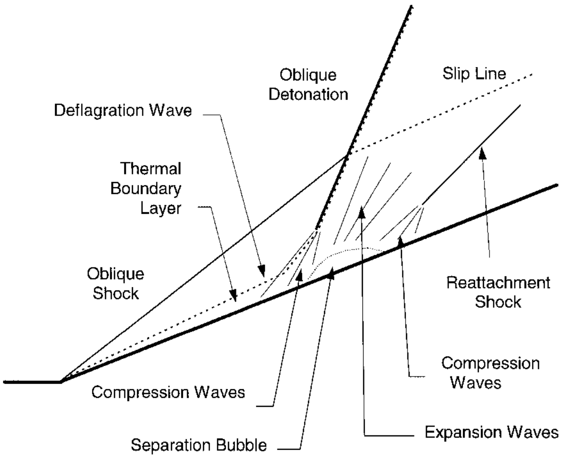

Fig. 10 Schematic of flow structure of stabilized oblique detonation supported by strong shock wave/boundary-layer interaction.

For the mixtures considered here, the induction length behind the incidence shock is probably much larger than the distance from the nose to the position of oblique detonation, because the oblique detonation has not existed at the earlier stage but has propagated upstream as the reaction develops and burned gas expands. That is, the oblique detonation is not initiated by the incidence of oblique shock, but is supported by the separation bubble that acts as an obstacle such as a secondary cone. The small values of local Mach number and Reynolds number in the burned gas region could be the reason for the shock wave/boundary-layer interaction and the separation bubble, even though the velocity of projectile is very high.

Conclusion

A computational fluid dynamics code is developed to analyze the supersonic reacting flow in the ram accelerator. Unsteady numerical simulations are performed to clarify the superdetonative mode initiation process of the ram accelerator by considering the injection of the projectile from the launcher into the accelerator barrel. From the results of the simulations, the performance characteristics of the scram accelerator that were investigated experimentally are clearly explained by a series of visualized flowfield data. The distinctive features observed are summarized as follows.

In the regular operating condition, the ignition initiates at shock wave/boundary-layer interaction region and the main reaction front is composed of the oblique shock-induced combustion front and the normal detonation to the barrel wall. However, in more energetic mixtures, the shock wave/boundary-layer interaction induces a large separation bubble that may lead a new oblique detonation. The oblique detonation moves forward and is stabilized at the conical nose. The location of the oblique detonation is considered to be important because the frontal location of detonation causes the severe reduction of the thrust and sometime leads to a kind of lower dilution limit unstart if the location is upstream of the critical location.

For the most energetic mixture considered, the spontaneous initiation of oblique detonation is observed at the conical nose, and the thermal choking is caused by a large separation bubble, which is induced by a series of shock wave/boundary-layer interactions. Because of the thermal choking condition, the oblique detonation changes to a normal detonation and moves upstream. This result explains the experimentally observed unstart phenomena. As another extreme case, upper dilution limit unstart occurs when the heat addition is not sufficient to expand the reaction front to form a strong shock reflection at the rear part of the body. In this case, most of the high-density unburned mixture flows through the narrow region between the barrel wall and reaction front.

As mentioned, the viscous effect is considered to be very important because the viscous effect induces the complex flow interactions and also plays an important role in the stabilization mechanism of the oblique detonation. That is, the stabilization mechanism of oblique detonation in the ram accelerator is based on shock wave/boundary-layer interaction.

Acknowledgment

Authors would like to acknowledge the support by the Turbo and Power Machinery Research Center assigned by the Korea Science and Engineering Foundation.

References

[1] Hertzberg, A., Bruckner, A. P., and Bogdanoff, D. W., "Ram Accelerator: A New Chemical Method for Accelerating Projectiles to Ultrahigh Velocities," *AIAA Journal*, Vol. 26, No. 2, 1988, pp. 195–203.

[2] Bogdanoff, D. W., "Ram Accelerator Direct Space Launch System: New Concepts," *Journal of Propulsion and Power*, Vol. 8, No. 2, 1992, pp. 481–490.

[3] Bruckner, A. P., Knowlen, C., Herzberg, A., and Bogdanoff, D. W., "Operational Characteristics of the Thermally Choked Ram Accelerator," *Journal of Propulsion and Power*, Vol. 7, No. 5, 1991, pp. 828–836.

[4] Kruczynski, D. L., Liberatore, F., and Nusca, M. J., "Experimental Flow Visualization for a Large-Scale Ram Accelerator," *Journal of Propulsion and Power*, Vol. 12, No. 1, 1996, pp. 206–210.

[5] Liberatore, F., "One-Dimensional, Equilibrium Chemistry Ram Accelerator Performance Calculations," *Journal of Propulsion and Power*, Vol. 11, No. 6, 1995, pp. 1366–1368.

[6] Nusca, M. J., and Kruczynski, D. L., "Reacting Flow Simulation for a Large-Scale Ram Accelerator," *Journal of Propulsion and Power*, Vol. 12, No. 1, 1996, pp. 61–69.

[7] Li, C., Kailasanath, K., and Oran, E. S., "Stability of Projectiles in Thermally Choked Ram Accelerators," *Journal of Propulsion and Power*, Vol. 12, No. 4, 1996, pp. 807–809.

[8] Bogdanoff, D. W., Knowlen, C., Murakami, D., and Stonich, I., "Magnetic Detector for Projectiles in Tubes," *AIAA Journal*, Vol. 28, No. 11, 1990, pp. 1942–1944.

[9] Bogdanoff, D. W., "New Tube End Closure System for the Ram Accelerator," *Journal of Propulsion and Power*, Vol. 10, No. 4, 1994, pp. 518–521.

[10] Seiler, F., Patz, G., Smeets, G., and Srulijes, J., "The Rail Tube in a Ram Acceleration: Feasibility Study with ISL's RAMAC 30," Second International Workshop on Ram Accelerators, RAMAC II, Seattle, WA, July 1995; also Inst. of Saint-Louis, ISL Rept. PU366/95, St. Louis, France, 1995.

[11] Yungster, S., Eberhardt, S., and Bruckner, A. P., "Numerical Simulation of Hypervelocity Projectiles in Detonable Gases," *AIAA Journal*, Vol. 29, No. 2, 1991, pp. 187–199.

[12] Pratt, D. T., Humphrey, J. W., and Glenn, D. E., "Morphology of Standing Oblique Detonation Wave," *Journal of Propulsion and Power*, Vol. 7, No. 5, 1991, pp. 837–845.

[13] Powers, J. M., and Stewart, D. S., "Approximate Solutions for Oblique Detonations in the Hypersonic Limit," *AIAA Journal*, Vol. 30, No. 3, 1992, pp. 726–736.

[14] Li, C., Kailasanath, K., and Oran, E. S., "Stability of Oblique Detonations in Ram Accelerators," AIAA Paper 92-0089, Jan. 1992.

[15] Yungster, S., and Bruckner, A. P., "Computational Studies of a Superdetonative Ram Accelerator Mode," *Journal of Propulsion and Power*, Vol. 8, No. 2, 1992, pp. 457–463.

[16] Yungster, S., "Numerical Study of Shock-Wave/Boundary-Layer Interactions in Premixed Combustible Gases," *AIAA Journal*, Vol. 30, No. 10, 1992, pp. 2379–2387.

[17] Matsuo, A., Fujii, K., and Fujiwara, T., "Flow Features of Shock-Induced Combustion Around Projectile Traveling at Hypervelocities," *AIAA Journal*, Vol. 33, No. 6, 1995, pp. 1056–1063.

[18] Lefebvre, M. H., and Fujiwara, T., "Numerical Modeling of Combustion Processes Induced by a Supersonic Conical Blunt Body," *Combustion and Flame*, Vol. 100, No. 1/2, 1995, pp. 85–93.

[19] Choi, J.-Y., Jeung, I.-S., and Lee, S., "Dimensional Analysis of the Effect of Flow Conditions on Shock-induced Combustion," *Twenty-Sixth Symposium (International) on Combustion*, Combustion Inst., Pittsburgh, PA, 1996, pp. 2925–2932.

[20] Choi, J.-Y., Jeung, I.-S., and Yoon, Y., "Transient Simulation of the Superdetonative Mode Initiation Process in Scram Accelerator," *Twenty-Sixth Symposium (International) on Combustion*, Combustion Inst., Pittsburgh, PA, 1996, pp. 2957–2963.

[21] Strehlow, R. A., *Combustion Fundamentals*, McGraw–Hill, New York, 1984, p. 481.

[22] Gardiner, W. C., Jr., *Combustion Chemistry*, Springer–Verlag, New York, 1984, pp. 485–504.

[23] Buckwalter, D. L., Knowlen, C., and Bruckner, A. P., "Ram Accelerator Performance Analysis Code Incorporating Real Gas Effects," AIAA Paper 96-2945, July 1996.

[24] Li, C., Kailasanath, K., and Oran, E. S., "Detonation Structures Generated by Multiple Shocks on Ram-Accelerator Projectiles," *Combustion and Flame*, Vol. 108, No. 1/2, 1997, pp. 173–186.

[25] Bird, R. B., *Transport Phenomena*, Wiley, New York, 1960.

[26] Shuen, S., and Yoon, S., "Numerical Study of Chemically Reacting Flows Using a Lower-Upper Symmetric Successive Overrelaxation Scheme," *AIAA Journal*, Vol. 27, No. 12, 1989, pp. 1752–1760.

[27] Moretti, G., "A New Technique for the Numerical Analysis of Nonequilibrium Flows," *AIAA Journal*, Vol. 3, No. 2, 1965, pp. 223–229.

[28] Evans, J. S., and Schexnayder, C. J., "Influence of Chemical Kinetics and Unmixedness on Burning in Supersonic Hydrogen Flames," *AIAA Journal*, Vol. 18, No. 2, 1980, pp. 188–193.

[29] Lee, S. H., and Deiwert, G. S., "Flux-Vector Splitting Calculation of Nonequilibrium Hydrogen–Air Reactions," *Journal of Spacecraft and Rockets*, Vol. 27, No. 2, 1990, pp. 167–174.

[30] Choi, J.-Y., Jeung, I.-S., and Cho, K. K., "Numerical Analysis of Shock-Induced Combustion Using Higher Order Upwind LU-SSOR Scheme," *Journal of Korean Society of Aeronautical and Space Sciences*, Vol. 22, No. 6, 1994, pp. 15–24.

[31] Jachimowski, C. J., "An Analytical Study of the Hydrogen-Air Reaction Mechanism with Application to Scramjet Combustion," NASA TP-2791, Feb. 1988.

[32] Baldwin, B. S., and Lomax, H., "Thin Layer Approximation and Algebraic Model for Separated Turbulent Flow," AIAA Paper 78-257, Jan. 1978.

[33] Drummond, J. P., "Supersonic Reacting Internal Flowfields," *Numerical Approaches to Combustion Modeling*, edited by E. S. Oran and J. P. Boris, AIAA, Washington, DC, 1991, pp. 365–420.

[34] Roe, P. L., "Approximate Riemann Solvers, Parameter Vectors, and Difference Schemes," *Journal of Computational Physics*, Vol. 43, 1981, pp. 357–372.

[35] Grossman, B., and Cinnella, P., "Flux Split Algorithms for Flows with Non-equilibrium Chemistry and Vibrational Relaxation," *Journal of Computational Physics*, Vol. 88, 1990, pp. 131–168.

[36] Jeon, H., Byun, Y., and Rho, O., "Numerical Analysis of Thermal and Chemical Nonequilibrium Flow Using Upwind Scheme," *Journal of Korean Society of Aeronautical and Space Sciences*, Vol. 20, No. 4, 1992, pp. 1–13.

[37] Montagne, J. L., Yee, H. C., Klopfer, G. H., and Vinokur, M., "Hypersonic Blunt Body Computation Including Real Gas Effects," NASA TM 10074, March 1988.

[38] Hirsch, C., *Numerical Computation of Internal and External Flows*, Vol. 2, Wiley, New York, 1990, Chap. 21.

[39] Morris, C. I., Kamel, M. R., and Hanson, R. K., "Expansion Tube Investigation of Ram-Accelerator Projectile Flow Fields," AIAA Paper 96-2680, July 1996.

[40] Choi, J.-Y., Jeung, I.-S., and Yoon, Y., "Structure of Stabilized Oblique Detonation Wave in Ram Accelerator," *Proceedings of The Asia-Pacific Conference on Combustion, ASPACC* (Osaka, Japan), 1997, pp. 452–459.

[41] Li, C., Kailasanath, K., and Oran, E. S., "Effects of Boundary Layers on Oblique-Detonation Structures," AIAA Paper 93-0450, Jan. 1993.

K. Kailasanath
Associate Editor